

RESEARCH ARTICLE | JUNE 24 2009

Revisiting the two first instabilities of the flow in an annular rotor-stator cavity

Sébastien Poncet; Éric Serre; Patrice Le Gal



Physics of Fluids 21, 064106 (2009)

<https://doi.org/10.1063/1.3156859>



APL Energy

Latest Articles Online!

Read Now



Revisiting the two first instabilities of the flow in an annular rotor-stator cavity

Sébastien Poncet,^{1,a)} Éric Serre,^{1,b)} and Patrice Le Gal^{2,c)}

¹Laboratoire M2P2, CNRS–Universités d’Aix-Marseille, UMR 6181, IMT La Jetée, Technopôle Château-Gombert, 38 Rue F. Joliot-Curie, 13451 Marseille Cédex 20, France

²IRPHE, CNRS–Universités d’Aix-Marseille, UMR 6594, Technopôle Château-Gombert, 49 Rue F. Joliot-Curie, B.P. 146, 13384 Marseille Cédex 13, France

(Received 28 January 2009; accepted 27 May 2009; published online 24 June 2009)

The stability of the flow enclosed between a stationary and a rotating disk with a central hub is revisited by experimental visualizations and direct numerical simulations in the case of unmerged boundary layers. The first instability appears as circular rolls, denoted by CRs (type 2 instability), which propagate along the stator before vanishing in the vicinity of the hub. The calculations highlight the convective nature of these rolls, which is in agreement with previous experimental results (P. Gauthier, P. Gondret, and M. Rabaud, *J. Fluid Mech.* **386**, 105 (1999)). It proves in particular that the CR instability observed in the experiment under permanent conditions is noise sustained. Above a second threshold, spiral rolls, denoted SR1 (type 1 instability), appear at the periphery of the cavity and can coexist with the circular rolls. The DNS shows that they appear through a supercritical Hopf bifurcation. The SR1 patterns appear to be very close to those emitted by the corner vortices obtained by Lopez and Weidman [*J. Fluid Mech.* **326**, 373 (1996)] during the spin-down of a rotating disk in a fixed cylinder. © 2009 American Institute of Physics.

[DOI: 10.1063/1.3156859]

I. INTRODUCTION

The stability of the flow confined between a rotating (rotor) and a stationary (stator) disk is mainly governed by two global parameters:¹ the aspect ratio $G=h/b$ of the cavity and the rotational Reynolds number $Re=\Omega b^2/\nu$, where h is the interdisk spacing, b is the rotating disk radius, and Ω is the rotation rate. In such rotating disk cavity, two types of instability have been identified: type 1 instability results from an inviscid mechanism due to unstable inflection points in the boundary layer velocity profiles, whereas type 2 instability is viscous and associated with the Coriolis terms. Itoh *et al.*² observed experimentally that the first instabilities occur in the stator boundary layer, which is confirmed by the linear stability analysis (LSA) of San'kov and Smirnov³ and Serre *et al.*⁴ and also by the direct numerical simulation (DNS) of Serre *et al.*⁵ The transition to turbulence in a cylindrical rotor-stator cavity was considered later by Schouveiler *et al.*^{6,7,1} Their experiments reported that, for $G>0.071$, the two first stages of the transition are due to the developments of instabilities in the stator boundary layer. Above a first threshold, they observed the formation of circular rolls (CRs) centered on the rotation axis, which propagate towards the center of the cavity. The CR instability, which is a type 2 instability has been formerly observed by Savas^{8,9} during the spin-down of a rotating disk and later by Schouveiler *et al.*^{1,6,7} and Gauthier *et al.*¹⁰ under permanent conditions. Above a second threshold, Schouveiler *et al.*^{1,6,7} observed spiral rolls (SR1), which appear at the periphery of

the cavity and coexist with the CR instability. The SR1 patterns are a type 1 instability with a band of stable modes limited by the Eckhaus secondary instability. Their radial wavelength strongly varies between DNS results (between 4.4 and 14.7 for $G=0.2$) and the results of a LSA (between 21.2 and 24.35),⁴ which has to be addressed in the present work. When the Reynolds number is increased further, a transition to a kind of wave turbulence occurs.¹¹ Gauthier *et al.*¹⁰ showed, by flow visualizations, that the CRs are very sensitive to an external (un)controlled forcing and then highlighted the convective nature of this instability.

Numerous experimental,^{1,2,6,7,10} theoretical,³ or numerical^{4,5} works have already been dedicated to the stability of the flow with unmerged boundary layers corresponding to $G>0.071$. Nevertheless, the nature of both the circular and spiral rolls remains unclear. The scenario first proposed by Schouveiler *et al.*¹ for the transition to turbulence in the enclosed rotor-stator cavity is revisited in the present paper essentially by numerical experiments using DNS but also by experimental flow visualizations in an annular cavity with a central hub.

II. EXPERIMENTAL SETUP

The cavity (Fig. 1) consists of two smooth parallel disks enclosed by an inner rotating cylinder (hub) of radius a and an outer stationary casing (shroud) of radius $b+j$ = 140.85 mm. In the experiments, various hubs have been tested: $a=6.5, 40, 55$, and 75 mm. The lower disk of outer radius $b=140\pm0.05$ mm is rotating (rotor), while the upper disk is stationary (stator). The interdisk space h is equal to 16 ± 0.02 mm. Thus, the value of the aspect ratio $G=h/b$ is here fixed to $G=0.114$, whereas the curvature parameter

^{a)}Electronic mail: poncet@l3m.univ-mrs.fr. Fax: 33.4.91.11.85.02.

^{b)}Electronic mail: serre1@l3m.univ-mrs.fr.

^{c)}Electronic mail: legal@irphe.univ-mrs.fr. Fax: 33.4.96.13.97.09.

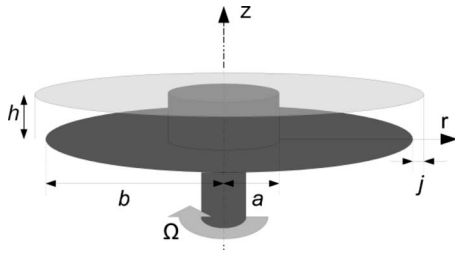


FIG. 1. Schematic representation of the annular rotor-stator cavity with relevant notation.

$R_m = (b+a)/(b-a)$ varies between 1 for a cylindrical cavity and 3.308 for the narrowest annular cavity. The rotor and the hub rotate clockwise at the same uniform rotation rate Ω with an accuracy of 0.2%. The shroud is fixed. The cavity is filled up with water maintained at a working temperature of 20 ± 0.1 °C and seeded with reflective particles of kalliroscope ($30 \times 6 \times 0.07 \mu\text{m}^3$) in order to visualize the hydrodynamic structures. This implies an accuracy better than 0.7% on the rotational Reynolds number $\text{Re} = \Omega b^2 / \nu$. Images (768×576 pixels) are taken at a video frequency of 25 images/s using a charge coupled device video camera. More details about the experimental setup can be found in Refs. 11 and 12.

III. NUMERICAL MODELING

The numerical approach is based on a pseudospectral technique using a collocation-Chebyshev method in the radial r and axial z nonhomogeneous directions and a Galerkin-Fourier method in the azimuthal periodic direction θ . Thus, each dependent variable $f = (V_r, V_\theta, V_z, P)$ is expanded into a truncated trigonometric series on T_n and T_m , a Chebyshev polynomial basis of degrees n and m , respectively. This approximation is applied at the Gauss-Lobatto collocation points, where the differential equations are assumed to be satisfied exactly, defined as $r_i = \cos(i\pi/N)$ for $i \in [0, N]$ and $z_j = \cos(j\pi/M)$ for $j \in [0, M]$ in the radial and axial directions. It ensures an accurate description of the solution in the very thin wall boundary layers.¹³ In the azimuthal direction, a uniform distribution is considered: $\theta_k = 2k\pi/K$ for $k \in [0, K]$. N and M define the number of collocation points in the radial and axial directions, respectively, and K is the cutoff in the tangential direction. A grid resolution composed of $73 \times 49 \times 100$ mesh points, respectively, in the radial, axial, and azimuthal directions is sufficient to get grid independent solutions. In the meridional plane, the space variables $(r, z) \in [a, b] \times [0, h]$ have been normalized into the square $[-1, 1] \times [-1, 1]$, a prerequisite for the use of Chebyshev polynomials.

The time scheme is semi-implicit and second order accurate. It is a combination of an explicit treatment of the convective terms (Adams-Bashforth scheme) and of an implicit treatment for the diffusive terms (second order backward Euler scheme). The dimensionless time step has been set to $\delta t = 10^{-3}$ in the present case. The solution method is based on an efficient projection scheme to solve the coupling between velocity and pressure. This algorithm ensures a

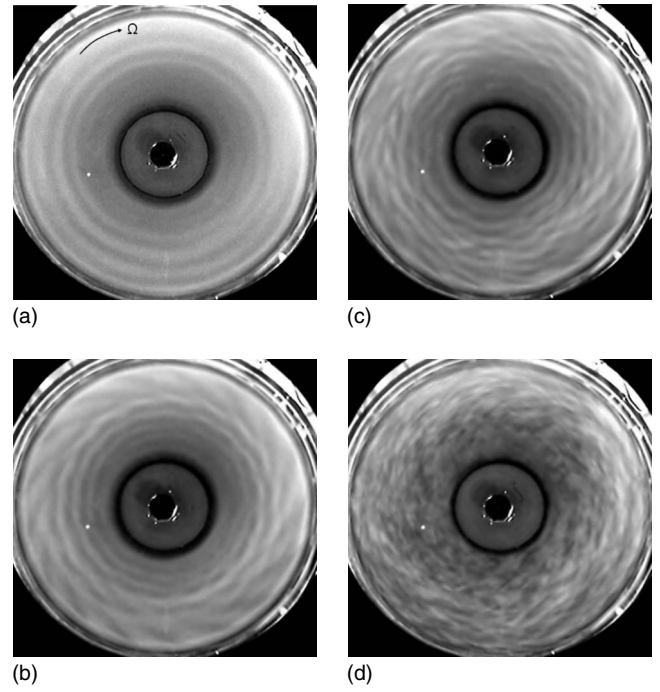


FIG. 2. Experimental flow visualizations for $G=0.114$, $R_m=1.8$ and (a) $\text{Re}=16\,400$, (b) $\text{Re}=24\,600$, (c) $\text{Re}=32\,500$, and (d) $\text{Re}=61\,600$.

divergence-free velocity field at each time step, maintains the order of accuracy of the time scheme for each dependent variable and does not require the use of staggered grids. Finally, for each Fourier mode, a full diagonalization technique is used and yields simple matrix products for the solution of successive two-dimensional uncoupled Helmholtz and Poisson equations at each time step.

The initial condition corresponds to a fluid at rest. No-slip boundary conditions are applied to all walls. There, $V_r = V_z = 0$ on all walls, whereas V_θ is fixed at zero on the stator and the shroud and at the local disk velocity Ωr on the rotor and the hub. The singularities present in the experiments at the junctions between rotating and stationary walls are regularized in the DNS code by using an exponential function to provide a smooth switchover. This function provides a reasonable representation of experimental conditions, while retaining spectral accuracy.

IV. RESULTS

A. Influence of the curvature parameter on the stability of rotor-stator flows

Figure 2 shows some experimental visualizations of the flow from above the stator for $G=0.114$, $R_m=1.8$, $j=0.85$ mm, and various Reynolds numbers in the range $16\,400 \leq \text{Re} \leq 61\,600$. Note that for the range of parameters investigated, the flow along the rotating disk remains stable. These new visualizations above the stator confirm the scenario proposed by Schouveiler *et al.*^{1,6,7} for the transition to turbulence in a cylindrical rotor-stator cavity (without central hub) in the case of unmerged boundary layers. For this aspect ratio, the flow remains stable until the appearance of CRs [Fig. 2(a)] above a first threshold $\text{Re}_{c1} = 12\,300$ (Re_{h1}

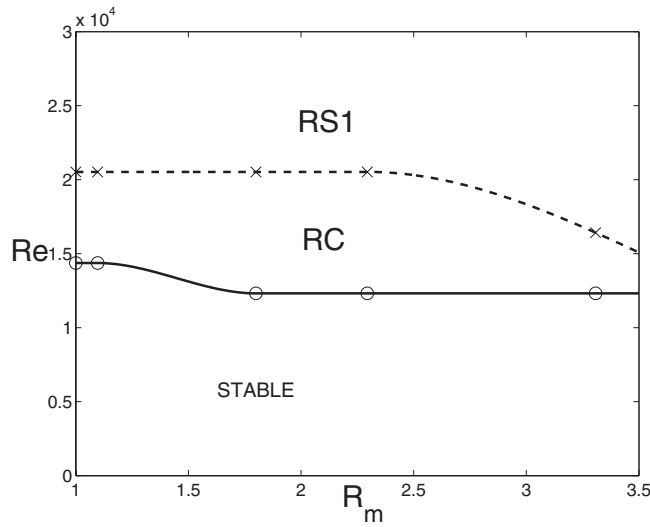


FIG. 3. Stability diagram of the flow with unmerged boundary layers in the plane (R_m, Re) deduced from the experiments in a rotor-stator cavity with a central hub for $G=0.114$.

$=Re\ G^2=160$, $Re_{\delta 1}=(\Omega r_c^2/\nu)^{1/2}=63$, with r_c the critical radial location for the appearance of the patterns), which is in excellent agreement with the value $Re_{c1}=12\ 000$ obtained by these authors^{1,6,7} for $G=0.114$, $R_m=1$, and $j=0$. Note that Serre *et al.*⁴ obtained lower values by DNS ($25.8 \leq Re_{\delta 1} \leq 62$ for $G=0.2$ and $R_m=1$ without any perturbation) and with their LSA for type II instability in the stator boundary layer: $34.7 \leq Re_{\delta 1} \leq 62$. Above a second threshold $Re_{c2}=20\ 500$ ($Re_{h2}=267$, $Re_{\delta 2}=100$), the SR1 instability [Figs. 2(b) and 2(c)] appear along the stator at the periphery of the cavity and coexist with the CR instability. This value matches with the experimental one of Cros *et al.*¹¹ for $G=0.114$, $R_m=1$, and $j=0.46$ mm. Buisine *et al.*¹⁴ obtained similar spiral waves by numerical simulation with additional perturbations for $Re_{h2} > 228$ and without any perturbation for $Re_{h2} > 400$ ($G=0.114$ and $R_m=1.857$). The value $Re_{\delta 2}=100$ obtained in the experiment remains in the range $47.5 \leq Re_{\delta 2} \leq 200$ obtained by LSA for type I instability in the stator boundary layer. In the experiment, when one increases further the Reynolds number, a transition to a kind of wave turbulence [Fig. 2(d)] appears for $Re \geq 41\ 000$ (see Ref. 11 for more details).

The influence of the parameter R_m on the stability diagram, in a (R_m, Re) plane, of the flow with unmerged boundary layers is presented in Fig. 3 for $G=0.114$. The thresholds of appearance of the CR and SR1 patterns, which are both permanently observed, are very weakly shifted to lower values of Re compared to the basic case with no inner cylinder ($R_m=1$), when R_m is increased. There are two possible reasons for that. First, the rotating hub connects the rotating and the stationary disks, which creates a stronger shear for the flow along the stator coming from the outer radii, than if the hub was stationary. Second, the main effect of the inner rotating cylinder, which increases with R_m , is to speed up the local fluid rotation rate Ω_f in the core of the flow and so, for a same value of Ω or Re , it slightly accelerates the transition to the SR1 regime. It can be seen as a “Rossby effect,” the

Rossby number Ro being defined as $Ro=\Omega_f/\Omega$. Note that the effect of the curvature parameter R_m remains weak compared to the effect of a forced inward throughflow¹² for instance.

The main characteristics of these two instabilities deduced from the experiments are given below for $G=0.114$, $R_m=1.8$, and $j=0.85$ mm. The CR frequency f_{CR}/Ω , which increases with the radial location because of successive pairings,⁶ remains in the range $[0.32-0.35]$ at $r^*=r/b=0.53$ whatever Re for $R_m=1.8$, in agreement with the value 0.32 of Cros *et al.*¹¹ for $G=0.114$, $R_m=1$, and $j=0.46$ mm. The mean critical radial location r_{CR}^* for the disappearance of the CR, in the range $Re=[(1.5 \times 10^4)-(4 \times 10^4)]$, is around 0.4. Thus, $Re_{\delta 1}$ varies between 52 and 109. The number of CRs, denoted by k_{CR} , varies strongly with Re from 3 at the threshold to 6 just before the appearance of the spiral waves. It confirms the value $k_{CR}=6$ obtained by Ref. 11 for $Re=18\ 500$. Then, k_{CR} remains equal to 4 for a wide range of Re values and decreases for $Re \geq 3.5 \times 10^4$ until their disappearance.

The critical radius r_{SR1}^* of appearance of the SR1 patterns slightly increases from 0.71 at $Re=20\ 500$ to 0.81 at $Re=41\ 000$. For the same set of parameters ($G=0.114$, $R_m=1.8$, and $j=0.85$ mm), the frequency of the spirals f_{SR1}/Ω remains almost constant in the range $[0.32-0.36]$ at $r^*=0.867$ for $Re=[20\ 500-41\ 000]$. As the magnitude of the mean tangential flow increases with the disk rotation rate reflected in the Re values, the angle ε_{SR1} of the spirals with the tangential direction decreases with increasing values of Re from 31° at threshold to 28° for $Re=24\ 600$ and finally to 24° for $Re=41\ 000$. The number of spiral arms k_{SR1} increases with rotation. $k_{SR1}=17$ up to $Re \approx 2.95 \times 10^4$ and increases to 18 for Re up to 3.8×10^4 then to 19 for larger Re values. Finally, the phase velocity V_ϕ of the spirals is positive: $V_\phi/(\Omega b)=0.101$ for $Re=24\ 600$ at $r^*=0.867$. The results concerning the spirals are in good agreement with the previous results of Cros *et al.*¹¹ for $G=0.114$, $R_m=1$, and $j=0.46$ mm: $f_{SR1}/\Omega=0.334$ and $\varepsilon_{SR1} \approx 25^\circ$ for $Re=24\ 600$.

B. Nature of the circular and spiral patterns

These new experiments using a central hub have shown that the scenario proposed by Schouveiler *et al.*¹ for the transition to turbulence in a cylindrical ($R_m=1$) rotor-stator cavity as well as the main characteristics of the two instabilities remain almost the same in the case of an annular cavity ($R_m=1.8$). The nature of these circular and spiral waves is now investigated in more details using DNS for the annular cavity defined by $G=0.114$ and $R_m=1.8$ already considered experimentally.

1. Circular rolls (CRs)

The DNS is initialized using conditions corresponding to a fluid at rest. Then the Reynolds number is increased regularly until the appearance threshold Re_{c1} of the CR instability. Whatever the spin-up to reach this threshold and without any spatial perturbation, Re_{c1} remains in the range $[10\ 000-10\ 500]$ by DNS ($28.6 \leq Re_{\delta 1} \leq 29.3$), while they are visible from $Re_{c1}=12\ 300$ in the experiment. The numerical values

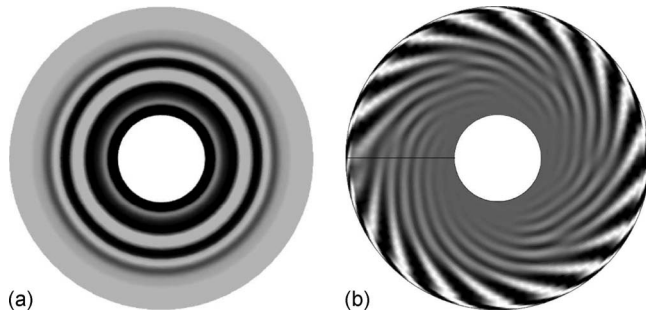


FIG. 4. Isovalues of the instantaneous axial component V_z of the velocity vector obtained by DNS for $G=0.114$ and $R_m=1.8$ at $z^*=0.86$ showing (a) the circular waves for $Re=15\,000$ at $t^*=3.83$ and (b) the spiral waves for $Re=24\,630$ at $t^*=175.9$ ($A=0.2, k=5$).

are in close agreement with previous DNS ($Re_{\delta l}=27$) of Serre *et al.*⁵ for $G=0.2$ and $R_m=1$. The LSA of Serre *et al.*⁴ showed that the stator boundary layer is convectively unstable for $Re_{\delta} \geq 34.7$, which corresponds also to the appearance threshold for the type II instability. This weak discrepancy between the LSA of Serre *et al.*⁴ and the present DNS results may be attributed to a Rossby effect. Indeed, the LSA has been performed for $Ro=0.313$ corresponding to Batchelor flows between infinite disks, whereas the Rossby number varies in the present calculations between 0.34 and 0.53 far from the cylinders. The stator boundary layer is then more stable when the Rossby number is increased in agreement with Serre *et al.*⁴ Figures 4(a) and 5(a) present the isovalues of the instantaneous axial velocity V_z in the stator boundary layer and some isocontours of V_z in a (r^*, z^*) plane, respectively, for $Re=15\,000$ at $t^*=3.83$ (t^* is a dimensionless time corresponding to the number of disk turns). It reveals that the CRs appear in the Stewartson layer attached to the external fixed cylinder [Fig. 5(a)] and moves along the stator towards

the rotation axis with a negative phase velocity $V_{\phi}/(\Omega b) = -0.143$ at $(r^*=0.604, z^*=z/h=0.611)$. Previous measurements of Schouveiler *et al.*⁷ using an ultrasonic Doppler anemometer showed that the CR occupies the half upper part of

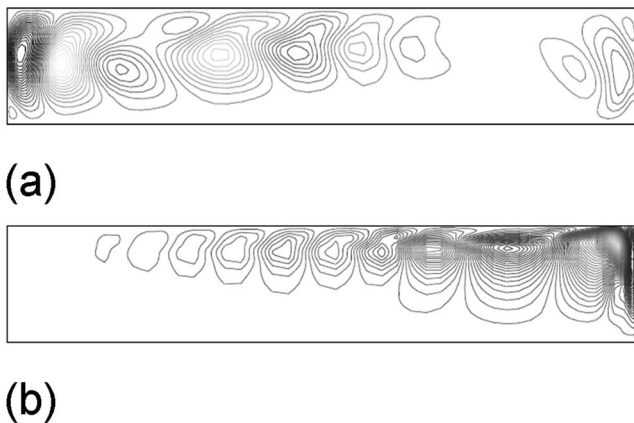


FIG. 5. Isovalues of the instantaneous axial component V_z of the velocity vector obtained by DNS for $G=0.114$ and $R_m=1.8$ in a (r^*, z^*) plane: (a) the CR patterns for $Re=15\,000$ at $t^*=3.83$ and (b) the SR1 spirals for $Re=24\,630$ at $t^*=175.9$ ($A=0.2, k=5$). $r^* \in [0.286, 1]$ and $z^* \in [0, 1]$.

the cavity and that for $Re=17\,200$, $G=0.114$, $R_m=1$, and $j=0$, they propagate with a negative phase velocity equal to -0.032 at $r^*=0.57$. This difference for V_{ϕ} may be attributed to the presence of the hub that accelerates the poloidal circulation of the flow, the CRs being advected by the secondary inward throughflow passing along the stator. Note that the axial extent of the CR increases when approaching the hub. For $r^*=0.693$, they are confined between $z^*=0.4$ and $z^*=0.933$, whereas, very close to the hub, the CR occupies about 90% of the interdisk spacing. The number of CRs $k_{CR}=4$ remains the same in the experiment and in the DNS for $Re=10\,500$ and the CR frequency obtained numerically $f_{CR}/\Omega=0.318$ is in excellent agreement with the experimental value ($f_{CR}/\Omega=0.32$).

Nevertheless, there is one main difference between the two approaches. Figure 7(a) shows the space-time diagram of the dimensionless mean axial velocity $V_z^* = V_z/(\Omega r)$ along a given circle ($0 \leq \theta^* = \theta/(2\pi) \leq 1$) at $r^*=0.604$ and $z^*=0.812$ for $Re=24\,630$. It reveals that, for this value of Re , the CRs, which appear on this figure as vertical black and white stripes, disappear after 20 disk turns. For $Re=15\,000$, they disappear after only ten disk turns. These ten disk turns correspond in fact to the spin-up time $\tau = O(E^{-1/2}\Omega^{-1})$ introduced by Weidman,¹⁵ with $E = \nu/(\Omega h^2)$ the Ekman number: $t^*=10 \approx 4.05 \times E^{-1/2}\Omega^{-1}$. It supports also the observations of Savas⁹ during the spin-down of a single rotating disk enclosed by an outer fixed cylinder. Moreover, it confirms the conclusions of Gauthier *et al.*¹⁰ on the convective nature of this instability. Thus, the CR seems to be maintained in the present experimental setup by an experimental noise probably due to the driving belt of the electrical motor. We recall that Schouveiler *et al.*^{6,17} and then Cros *et al.*^{16,11} used the same device.

Some numerical calculations have been performed to show the sensibility of the CRs to the amplitude of a spin-up $\Delta\Omega = \Omega_1 - \Omega_0$ starting from the stable flow at $Re=10\,500$ ($\Omega_0=0.536$ rad/s). Figure 6 shows the duration time t^* (equivalent to the number of disk turns) of the CR patterns against $\Delta\Omega/\Omega_0$. The spin-up of the rotor can be seen as an axisymmetric perturbation of the base flow. When the amplitude of the spin-up increases, the disappearance of the CRs is delayed according to the interpolation law: $t^* = 2.5\Delta\Omega/\Omega_0 + 2.8$. These results are very similar to the numerical ones of Lopez and Weidman¹⁷ during the spin-down of a rotating disk in a stationary cylinder. They showed, in particular, that during the first radians of rotation, the end wall boundary layer has a structure very similar to Bödewadt and stator boundary layers. They obtained axisymmetric waves traveling radially inward in this boundary layer. They conjectured that these may be eigenmodes of the Bödewadt layer.

2. Spiral rolls (SR1)

To highlight the nature of the SR1 instability, calculations have been performed for $Re=24\,630 > Re_{c2}=20\,525$ starting from the converged solution obtained at $Re=18\,473$ for which the flow remains stable. The values of G and R_m are still fixed to 0.114 and 1.8, respectively. Note that

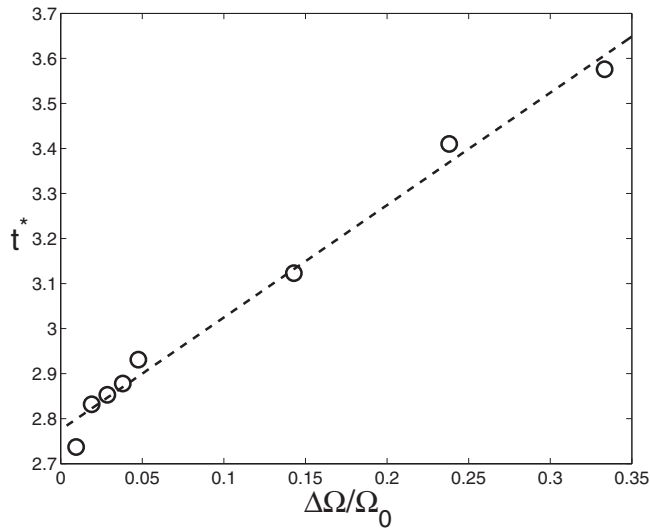


FIG. 6. Duration time t^* of the CR patterns vs a relative variation of rotation rate $\Delta\Omega = \Omega_1 - \Omega_0$ during the spin-up of the rotor. Plot obtained by DNS (circles) for $G=0.114$, $R_m=1.8$, and $\Omega_0=0.536$ rad/s ($Re=10\,500$) interpolated by $t^*=2.5\Delta\Omega/\Omega_0+2.8$ (dashed line).

the critical Reynolds number for the appearance of the SR1 patterns obtained by DNS is about $Re_{c2}=19\,781$ (see Fig. 9) in agreement with the experimental value $Re_{c2}=20\,500$. It corresponds to $Re_{\delta 2}=68$ close to the DNS results $Re_{\delta 2}=63.2$ of Serre *et al.*⁵ for $G=0.5$ and $R_m=1$. Two types of boundary condition for the tangential velocity imposed on the external cylinder have been considered: the first one (BC1) is a stationary cylinder with a small regularization at the corner between the rotor and the shroud ($V_\theta^* = \alpha e^{-z^*/\mu}$ with $\alpha=0.16$ and $\mu=0.003$). The second condition (BC2) corresponds to a linear profile for V_θ^* ($V_\theta^*=1-z^*$). Note that for cases 2, 3, and 4 defined below, the sinusoidal perturbation is applied to the axial velocity component such as $V_z = V_z[1 + A \sin(2i\pi/k)]$. Thus, the following scenarios have been considered (see Fig. 7):

- Case (1) BC1. We do not introduce any imposed sinusoidal perturbation.
- Case (2) BC1. A sinusoidal perturbation ($A=0.2$, $k=5$) is introduced at $t^*=62.8$.
- Case (3) BC2. The sinusoidal perturbation ($A=0.2$, $k=5$) is introduced at $t^*=62.8$.
- Case (4) Case 2 but at $t^*=175.9$, we switch to BC2.

For all cases, the jump in Reynolds number between $Re=18\,473$ and $Re=24\,630$ corresponding to the spin-up in the experiments of Savas⁹ first generates the CRs [see Figs. 7(a)–7(d)] already observed at lower Reynolds numbers. For case 1, they disappear after about 20 disk turns and then the flow becomes stationary. The SR1 patterns appear, without any imposed perturbation, after 290 disk turns. Figures 8(a) and 8(b) show the exponential growth of square root of the spectral energy $E_k(t)$ contained in each Fourier modes k of the velocity in the range $[15–19]$ and their first harmonic, respectively. The saturation of $E_k(t)$ is reached after around $t^*=310$. Mode 17 appears to be the most unstable mode in this configuration, close to the experimental value 18 ob-

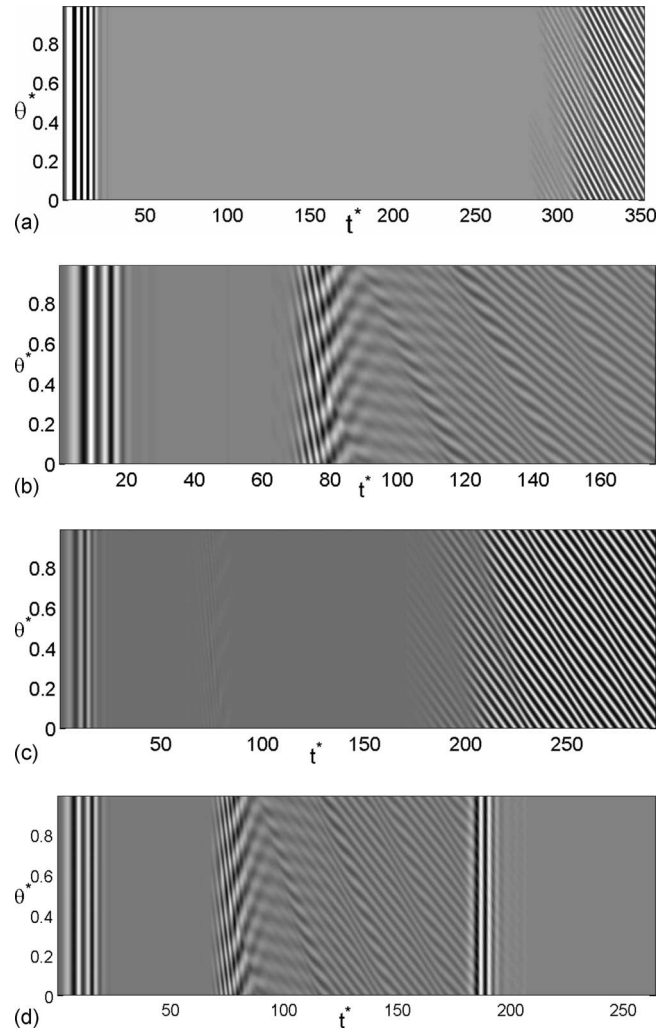


FIG. 7. Space-time diagrams of the axial velocity $V_z^* = \overline{V_z}/(\Omega r)$ deduced from the DNS for $Re=24\,630$, $G=0.114$, and $R_m=1.8$. $\theta^* = \theta/(2\pi)$ is the azimuthal angle on a fixed circle at $r^*=0.604$ and $z^*=0.812$. (a) Case 1, (b) case 2, (c) case 3, and (d) case 4.

tained by Schouveiler *et al.*⁶ for $G=0.114$ and $R_m=1$. This saturation is a classical non linear saturation as the slopes (in logarithmic scale) of the first harmonics [Fig. 8(b)] are twice steeper as the ones of the modes themselves [Fig. 8(a)]. It shows that this SR1 instability appear through a Hopf bifurcation. Figure 9 confirms the supercritical nature of the bifurcation observed by Schouveiler *et al.*⁶ and Cros *et al.*¹¹ as the spectral energy varies linearly with the Reynolds number. It provides also the value for the critical Reynolds number ($Re_{c2}=19\,781$) already invoked. We have measured the frequency of the spirals during their growth in order to obtain a nonlinear shift of this frequency. Amazingly, this frequency remains constant whatever the amplitude of the spirals is. It implies that the Landau constant associated with the Hopf bifurcation is equal to zero. Due to the periodicity of the flow in the azimuthal direction that implies a quantification of the azimuthal wavenumber k , it appears that k remains constant during the growth of the spirals (or at least during some lapse of time of this growth, see Fig. 7). As the frequency also remains constant (no nonlinear frequency shift), it means that the phase velocity of the SR1 pattern in the azimuthal direc-

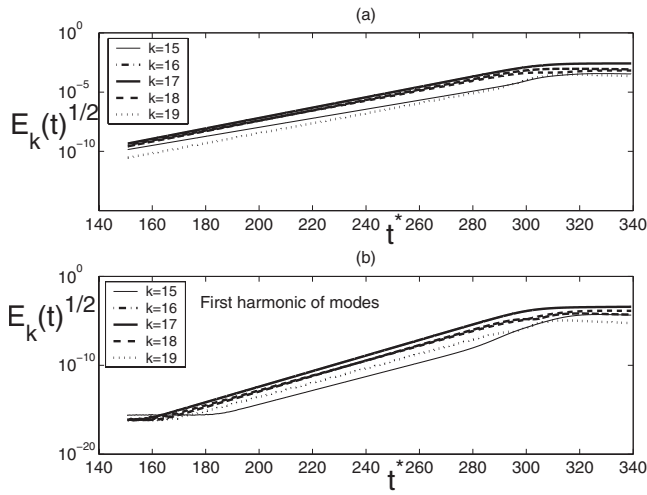


FIG. 8. Evolution with time of the square root of the spectral energy $E_k(t)$ contained in (a) each Fourier modes $k \in [15-19]$ and in (b) their first harmonic, for the SR1 waves. Plots obtained by DNS in case 1 for $Re = 24\,630$, $G = 0.114$, and $R_m = 1.8$.

tion is also constant. This can indeed be checked on the space-time diagrams of Fig. 7, where the spiral traces appear as rigorously straight lines. It suggests that the phase velocity of the waves may be locked to some hydrodynamical velocity independent of the amplitude of the waves.

Schouveiler *et al.*⁶ showed experimentally that the SR1 patterns are the subject to a secondary Eckhaus instability and thus, the wavenumber selection is very sensitive to the experimental procedure. To investigate its sensitivity and also to accelerate the transition to the SR1 spiral regime, the same calculation as the one described above is performed for the same parameters but a sinusoidal perturbation is introduced at $t^* = 62.8$. Its perturbation is applied to the axial velocity component V_z in the whole domain: $V_z = V_z[1 + A \sin(2\pi\theta/k)]$, where A is the amplitude of the perturbation and k is the azimuthal wavenumber. The space-time dia-

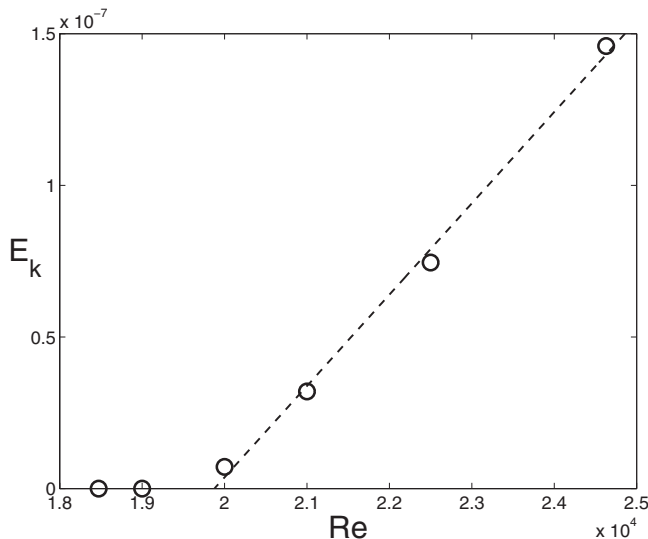


FIG. 9. Amplitude of the spectral energy E_k after the saturation contained in Fourier mode 17 vs the Reynolds number, obtained by DNS in case 1 for $Re = 24\,630$, $G = 0.114$, and $R_m = 1.8$.

gram corresponding to ($A = 0.2, k = 5$) is shown in Fig. 7(b). After a short transient state, 18 positive spiral arms [Fig. 4(b)] appear along the stator [Fig. 5(b)]. The amplitude of the perturbation is strong enough to speed up and control the transition process to the SR1 regime. From the 128 isocontours of the instantaneous axial velocity V_z in a (r, z) plane [Fig. 5(b)], it can be seen the decrease of the spiral size in the axial direction when approaching the rotation axis. The frequency of the SR1 spirals $f_{SR1}/\Omega = 0.352$ and their angle with the tangential direction $\varepsilon = 26^\circ$ are in excellent agreement with the present experiments $f_{SR1}/\Omega = 0.34$ and $\varepsilon = 28^\circ$ also for $G = 0.114$ and $R_m = 1.8$.

In case 3 [Fig. 7(c)], the boundary condition 2 (BC2) corresponding to a linear profile for V_θ^* on the external cylinder is applied at $t^* = 0$. It means that the shear between the wall and the fluid in solid body rotation is reduced to approximately zero, as both rotate at approximately half the disk speed at midheight of the cavity. The increase in Reynolds number from 18 473 to 24 630 generates the CR patterns, which disappears after about 20 disk turns. The sinusoidal perturbation is applied at $t^* = 62.8$ and after a short transient state (five negative spiral arms with $\varepsilon = -7^\circ$ attached to the stator), the flow becomes stable again until $t^* \approx 175$. The SR1 appear progressively with time. Thus, this BC2 on the external cylinder has a strong stabilizing effect on the flow but do not annihilate totally their growth.

The results obtained in case 2 are used as initial conditions for case 4 [Fig. 7(d)]. At $t^* = 175.9$, we switch to BC2 on the external cylinder. This change in boundary condition acts as a spin-up at the periphery of the cavity and as a consequence, during a short transient state, CRs appear and move toward the center of the cavity. At $t^* = 201.1$, two CRs coexist with 16 positive spiral arms ($\varepsilon = 25^\circ$). At $t^* = 226.2$, the flow becomes stable again. This sudden change has a more effective stabilizing effect on the flow compared to case 3. The modulations observed in the space-time diagrams in Figs. 7(b) and 7(d) are due to the growth of modes $k = 17$ and $k = 19$ together, which are not negligible compared to the dominant mode $k = 18$ [Fig. 4(b)].

These two last numerical experiments (cases 3 and 4) show that by diminishing the shear between the mean flow in the core region and the end wall, the appearance of the spirals has been delayed. Moreover, it confirms that even if these spirals are due to the destabilization of the stator boundary layer, the perturbation at the origin of the SR1 is produced in the Stewartson layer attached to the shroud [see also Fig. 5(b)]. The structure of the Stewartson layer along the external cylinder is presented in Fig. 10 for case 1 at $t^* = 310$, for which the SR1 patterns are obtained. It shows in particular the thickening of that boundary layer, when the fluid flows from the rotor to the stator.

Buisine *et al.*¹⁴ presumed that the spiral patterns that they obtained for two values of $G = [0.114; 0.3]$ and $R_m = 1.857$ were generated at the corner between the stator and the shroud and were due to the change in direction of the secondary flow. In our cases, whatever the boundary condition applied to the end wall, the boundary layer attached to it is centrifugally unstable regarding the modified Rayleigh criterion of Leibovich and Stewartson¹⁸ for an inviscid axisym-

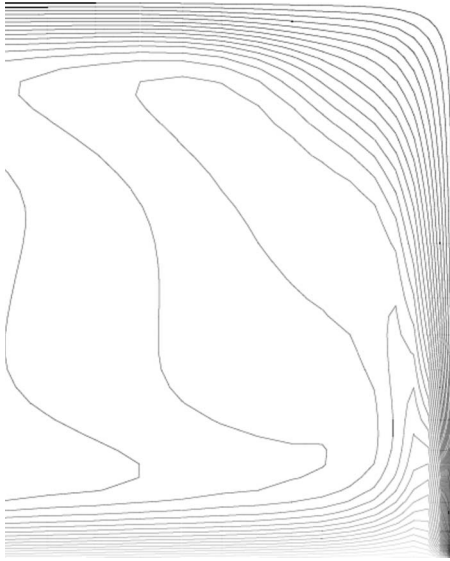


FIG. 10. Isocontours of the instantaneous tangential velocity at $t^*=310$ for $r^* \in [0.9, 1]$ and $z^* \in [0, 1]$ in case 1 ($Re=24\,630$, $G=0.114$, and $R_m=1.8$).

metric instability: $\Re a = V_\theta \partial_r \Omega [\partial_r \Omega \partial_r \Gamma + \partial_r V_z] < 0$, with $\Gamma = rV_\theta$ the circulation, $\Omega = V_\theta/r$ the angular velocity, and where ∂_r indicates the radial derivative. Figure 11 shows an example of isovalues of $\Re a$ for case 1 at $t^*=276.46$. This map matches with the numerical results of Lopez and Weidman¹⁷ for the impulsive spin-down problem of a rotating disk in a stationary cylinder. There are two main regions surrounded by zero $\Re a$ values: one region characterized by $\Re a > 0$ is situated at the corner between the stator and the cylinder and the other is just below with $\Re a < 0$. The SR1 spirals appear to be analog to the corner vortices obtained by Lopez and Weidman¹⁷ at the junction between the end wall and the stator. These authors showed that they are formed by the kinematics of the flow and that their formation is not controlled by a noise level in their calculation.

Several values for k , the selected Fourier mode, and A the amplitude of the sinusoidal perturbation have been com-

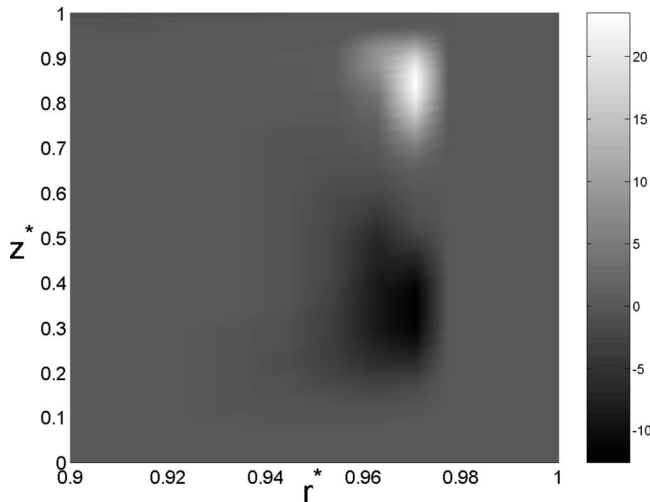


FIG. 11. Isovalues of $\Re a$ at $t^*=276.46$ in case 1 for $r^* \in [0.9, 1]$ and $z^* \in [0, 1]$ and for $Re=24\,630$, $G=0.114$, and $R_m=1.8$.

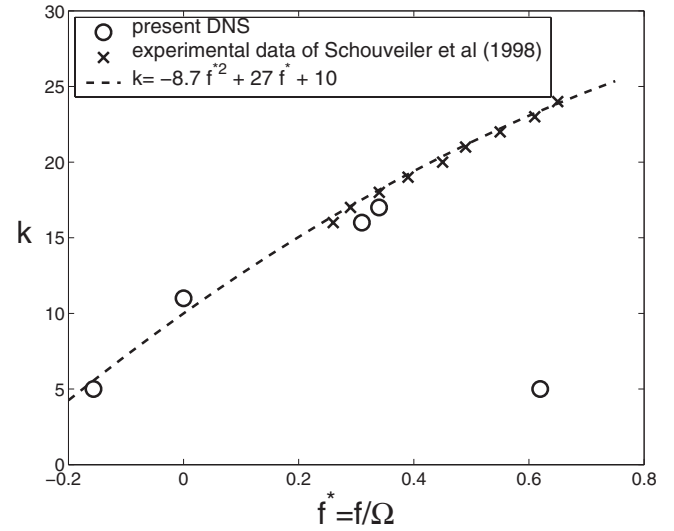


FIG. 12. Dispersion relation obtained by DNS for $Re=24\,630$, $G=0.114$, $R_m=1.8$, and $j=0.85$ mm and by experimental visualizations performed by Schouveiler *et al.* (Ref. 6) for $Re=25\,000$, $G=0.114$, $R_m=1$, and $j=0$.

puted. The main result is obtained for $(k=17, A=0.01)$. The 17 spiral waves are recovered, which shows that the flow is linearly unstable to such sinusoidal perturbation.

Finally, Fig. 12 presents the dispersion relation for the spiral waves. The present DNS results obtained for $Re=24\,630$, $G=0.114$, $R_m=1.8$, and $j=0.85$ mm are compared to the experimental data of Schouveiler *et al.*⁶ for $Re=25\,000$, $G=0.114$, $R_m=1$, and $j=0$. We calculate the normalized frequency $f^*=f/\Omega$ and the azimuthal wavenumber k of each mode from the transients observed in Fig. 7. As it can be observed, all the data collapse on the same dispersion relation curve, although modes computed by DNS have been only observed during transient states ($k=5, 11, 16$). All the data can be fitted by the following second order polynomial giving the azimuthal wavenumber k as a function of the spiral frequency f^* : $k = -8.7f^{*2} + 27f^* + 10$. The relation possesses a notable curvature and does not go through $(0,0)$, showing that the spiral propagation is dispersive. We note the presence of an isolated mode $k=5$ ($f^*=0.62$), which may belong to another branch of the dispersion relation. This illustrates the possibility of multiple solutions in the rotor-stator problem.¹⁹

V. CONCLUSION

A combined experimental and numerical study of the transition to turbulence of the flow in an annular rotor-stator cavity has been performed. We focused on the two instabilities, which occur in the case of unmerged boundary layer flow. The influence of the hub on the stability diagram has been investigated. It slightly increases the ratio between the fluid and the disk velocities (and so the Rossby number) but this effect remains weak. Then, flow visualizations and DNS results have been compared for $R_m=1.8$ and an excellent agreement has been obtained for the main characteristics of the circular and spiral rolls.

These two instabilities have been revisited using accurate DNS and the convective nature of the first instability,

which appears as CRs imbedded in the stator boundary layer, has been highlighted in agreement with previous results.¹⁰ Above a second threshold, a second instability appears as positive spiral patterns (SR1) also propagating along the stationary disk. Numerically and without any perturbation, mode $k=17$ appears to be the most unstable mode, in agreement with the results of Schouveiler *et al.*⁶ We have also shown that this mode saturates through the production of higher harmonics following the classical supercritical Hopf bifurcation picture. Whatever the boundary conditions on the end wall, the flow remains unstable according to the criterion of Leibovich and Stewartson.¹⁸ This end wall condition introduces a permanent perturbation, which destabilizes the stator boundary layer and induces the formation of the SR1 patterns, that propagate dispersively in the stator boundary layer.

ACKNOWLEDGMENTS

The authors acknowledge the IDRIS (CNRS, Orsay, France) computing center where the computations have been carried out on the NEC SX-8 supercomputer (program 070242).

¹L. Schouveiler, P. Le Gal, and M. P. Chauve, "Instabilities of the flow between a rotating and a stationary disk," *J. Fluid Mech.* **443**, 329 (2001).

²M. Itoh, Y. Yamada, and K. Nishioka, "Transition of the flow around an enclosed rotating disk," *Trans. Jpn. Soc. Mech. Eng., Ser. A* **51**, 452 (1985).

³P.I. San'kov and E.M. Smirnov, "Stability of viscous flow between rotating and stationary disks," *Mekh. Zhidk. Gaza* **6**, 79 (1991).

⁴E. Serre, E. Tuliska-Sznitko, and P. Bontoux, "Coupled numerical and theoretical study of the flow transition between a rotating and stationary

disk," *Phys. Fluids* **16**, 688 (2004).

⁵E. Serre, E. Crespo Del Arco, and P. Bontoux, "Annular and spiral patterns in flows between rotating and stationary discs," *J. Fluid Mech.* **434**, 65 (2001).

⁶L. Schouveiler, P. Le Gal, and M. P. Chauve, "Stability of a traveling roll system in a rotating disk flow," *Phys. Fluids* **10**, 2695 (1998).

⁷L. Schouveiler, M. P. Chauve, P. Le Gal, and Y. Takeda, "Spiral and circular waves in the flow between a rotating and a stationary disk," *Exp. Fluids* **26**, 179 (1999).

⁸O. Savas, "Circular waves on a stationary disk in rotating flow," *Phys. Fluids* **26**, 3445 (1983).

⁹O. Savas, "Stability of Bödewadt flow," *J. Fluid Mech.* **183**, 77 (1987).

¹⁰G. Gauthier, P. Gondret, and M. Rabaud, "Axisymmetric propagating vortices in the flow between a stationary and a rotating disk enclosed by a cylinder," *J. Fluid Mech.* **386**, 105 (1999).

¹¹A. Cros, E. Floriani, P. Le Gal, and R. Lima, "Transition to turbulence of the Batchelor flow in a rotor/stator device," *Eur. J. Mech. B/Fluids* **24**, 409 (2005).

¹²S. Poncet and M. P. Chauve, "Crossflow instability in a rotor-stator cavity with axial inward throughflow," *J. Fluid Mech.* **545**, 281 (2005).

¹³I. Raspo, S. Hugues, E. Serre, A. Randriamampianina, and P. Bontoux, "A spectral projection method for the simulation of complex three-dimensional rotating flows," *Comput. Fluids* **31**, 745 (2002).

¹⁴D. Buisine, F. Oble, and H. Andrianarainjaka, "Étude numérique des structures spirales tridimensionnelles à la périphérie d'une cavité interdisc," *C. R. Acad. Sci., Ser. IIb* **328**, 237 (2000).

¹⁵P. D. Weidman, "On the spin-up and spin-down of a rotating fluid. Part 1. Extending the Wedemeyer model," *J. Fluid Mech.* **77**, 685 (1976).

¹⁶A. Cros and P. Le Gal, "Spatiotemporal intermittency in the torsional Couette flow between a rotating and a stationary disk," *Phys. Fluids* **14**, 3755 (2002).

¹⁷J. M. Lopez and P. D. Weidman, "Stability of stationary endwall boundary layers during spin-down," *J. Fluid Mech.* **326**, 373 (1996).

¹⁸S. Leibovich and K. Stewartson, "A sufficient condition for the instability of columnar vortices," *J. Fluid Mech.* **126**, 335 (1983).

¹⁹N. Nguyen, J. P. Ribault, and P. Florent, "Multiple solutions for flow between coaxial disks," *J. Fluid Mech.* **68**, 369 (1975).